JOURNAL OF COMPUTATIONAL PHYSICS 111, 205–219 (1994)

A Divergence-Free Spectral Expansions Method for Three-Dimensional Flows in Spherical-Gap Geometries

GUY DUMAS* AND ANTHONY LEONARD

Graduate Aeronautical Laboratories, California Institute of Technology, Pasadena, California 91125

Received October 7, 1992; revised July 23, 1993

A spectral method for the solution of the incompressible Navier–Stokes equations in spherical-gap geometries is presented. The method uses divergence-free vector expansions which inherently satisfy the boundary conditions [1]. Basis and test functions are constructed from Chebyshev polynomials and vector spherical harmonics (VSH) yielding a Petrov–Galerkin weighted-residual method that produces spectral convergence. No rotational nor equatorial symmetry of the flow field is implicitly imposed. The approach makes extensive use of the convenient properties of the VSH which are presented in a computationally suitable form whenever possible. The alias-free implementation of the method rests upon a standard, explicit–implicit time-integration technique. A VSH–Chebyshev vector transform with two "fast directions" is also developed and briefly presented. Several test cases are used to validate the resulting initial-boundary-value code. Axisymmetric, basic spherical Couette flow computations are compared with available numerical results while a three-dimensional spiral Taylor–Görtler vortex flow simulation is tested against experimental measurements. Very good agreement is found in all cases.

1. INTRODUCTION

The purpose of this paper is to present the development and implementation of a specialized spectral method for the simulation of viscous incompressible flows in spherical-gap geometries. Such flows occur in the spacing between concentric spherical shells in differential rotation. Numerous phenomena encountered in those flows are of fundamental relevance to the understanding of global processes in planetary atmospheres and in the core of rotating stars [2]. The study of spherical-gap flows is also of basic importance in the field of hydrodynamic stability for it stands as a natural generalization of its more simple and classical analogues such as the plane and the circular Couette flows, and the flow between rotating disks [3].

Our motivation for the development of a new Navier–Stokes solver comes primarily from the physical studies aimed at, i.e., investigations of the transition and instability mechanisms in spherical Couette flows. From experimental results, it is known that the first transition in narrow-gap geometries involves spiraling Taylor-type vortices (e.g., [4]) while that in large-gap geometries shows traveling azimuthal waves of a complex structure [5]. For moderate-gap spherical Couette flows, both experimental and numerical studies agree that, although axisymmetric, the transition process as well as some super-critical steady solutions may be devoid of any form of equatorial symmetry [6, 7]. Therefore, the need for a fully three-dimensional method with no symmetry imposed is evident.

Among other requirements typical of transitional flow simulations, spectral accuracy as well as computational and memory efficiency were sought. In response to those requirements, the approach of Leonard and Wray [1] has been followed for the spatial discretization of the continuum equations. This approach has been the basis for the successful simulations of Leonard and Wray [1] for pipe flows, Moser *et al.* [8] for straight and curved channels, Spalart *et al.* [9, 38] for boundary layer, mixing layer, and wake flows, and Stanaway *et al.* [10] for axisymmetric vortex rings. For the spherical geometry, the availability of Hill's *Vector Spherical Harmonics* [11] alleviates the problem of two non-periodic directions by providing a natural, purely orthogonal, complete set of vector functions for the two angular directions (see also [39] for an alternative VSH basis in the context of vector elliptic equations). The threesome family of VSHs offers further attractive properties to be discussed below, e.g., analytical relations for the Laplacian operator and uniform resolution.

A description of the geometry and the flow parameters follows in Section 2. After a presentation of the foundations of the method in Section 3, the vector functions developed for the spherical and radial directions, as well as for the treatment of the non-homogeneous boundary conditions, are described in Section 4. Section 5 then discusses some aspects pertaining to the implementation of the method: the

* Current address: Department of Mechanical Engineering, Laval University, Québec, Canada G1K-7P4.

0021-9991/94 $6.00

time-integration scheme, the discrete transforms, the treatment of the nonlinear term and aliasing error. Finally, Section 6 presents some of the numerical tests that have been performed to assert the validity and efficiency of the method.

2. DESCRIPTION AND PARAMETERS

A fixed cartesian system of coordinates (x, y, z) is considered with the z-direction aligned with the axis of rotation of the inner sphere and further positioned so that the axis of rotation of the outer shell lies entirely in the x-z plane, as depicted on Fig. 1. Introducing standard polar spherical coordinates (r, θ, ϕ) with *radial*, *polar*, and *azimuthal* directions and unit vectors $(\hat{\mathbf{e}}_r, \hat{\mathbf{e}}_\theta, \hat{\mathbf{e}}_\phi)$, it is a simple matter to determine the velocity boundary conditions on each sphere $(\bar{\mathbf{u}} = \bar{\boldsymbol{\Omega}} \times \bar{\mathbf{x}})$:

$$\bar{\mathbf{u}}(\bar{r} = \bar{R}_i, \theta, \phi) = \bar{\Omega}_i \bar{R}_i \begin{pmatrix} 0 & \hat{\mathbf{e}}_r \\ 0 & \hat{\mathbf{e}}_\theta \\ \sin\theta & \hat{\mathbf{e}}_\phi \end{pmatrix}$$

$$\bar{\mathbf{u}}(\bar{r} = \bar{R}_o, \theta, \phi) = \bar{\Omega}_o \bar{R}_o \begin{pmatrix} 0 & \hat{\mathbf{e}}_r \\ -\sin\alpha_o \sin\phi & \hat{\mathbf{e}}_\theta \\ \cos\alpha_o \sin\theta - \sin\alpha_o \cos\theta \cos\phi & \hat{\mathbf{e}}_\phi \end{pmatrix}, \tag{1}$$

where $\bar{R}_i$, $\bar{R}_o$, $\bar{\Omega}_i$, and $\bar{\Omega}_o$ are respectively the inner and outer radius and angular velocity, while α_o is the polar angle (θ-direction) between the vertical z-direction (also the $\bar{\Omega}_i$-axis) and the $\bar{\Omega}_o$-axis. The bar superscript "$-$" is used here to identify dimensional quantities.

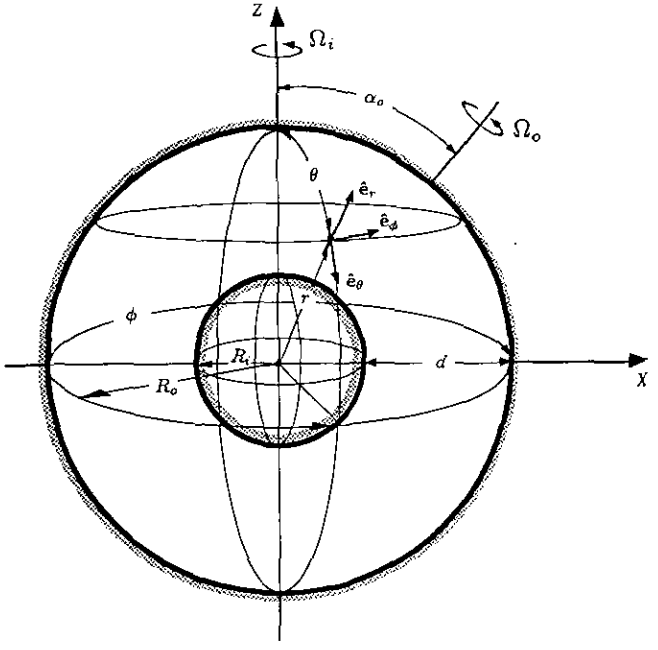

FIG. 1. Sperical-gap flow geometry and coordinates. The Ω_i-axis of rotation is in the z-direction while the Ω_o-axis lies in the x-z plane with a polar angle α_o.

One notes that while the velocity on the inner sphere can only be azimuthal, the velocity on the outer shell always involves both polar and azimuthal components except for the particular case of *spherical Couette flows* for which the two axes coincide, and therefore $\alpha_o = 0$. In addition, for the sake of generality, one also allows for $\bar{\Omega}_i$, $\bar{\Omega}_o$ and α_o to be arbitrary, known functions of time. It will be convenient for future reference to define the following quantities:

$$\begin{aligned} \bar{d} &\equiv \bar{R}_0 - \bar{R}_i && \text{gap width,} \\ \delta &\equiv \bar{d}/\bar{R}_i && \text{relative gap size,} \\ \bar{V}_i &\equiv \bar{\Omega}_i \bar{R}_i && \text{inner-wall speed,} \\ \bar{V}_o &\equiv \bar{\Omega}_o \bar{R}_o && \text{outer-wall speed.} \end{aligned} \tag{2}$$

In order to express all physical variables in dimensionless form, a reference length $(\bar{L}_r = \bar{d})$ and reference velocity $(\bar{V}_r = \bar{V}_i$ or $\bar{V}_o$ according to the specific problem) are chosen. If time-dependent boundary conditions are used, the maximum value of $\bar{V}_i$ or $\bar{V}_o$ would be chosen. The Reynolds number is $\mathrm{Re} = \bar{V}_r \bar{L}_r / \bar{\nu}$.

In summary, for the most general case, one needs to specify five parameters to completely define the problem: one geometric parameter "δ," one equation parameter "Re," and three time-dependent boundary parameters "$\alpha_o(t)$" and dimensionless "$V_i(t)$" and "$V_o(t)$."

3. WEIGHTED-RESIDUAL METHOD

The dimensionless Navier–Stokes equations for incompressible flow consist of the momentum equation

$$\frac{\partial \mathbf{u}}{\partial t} + \mathbf{u} \cdot \nabla \mathbf{u} = -\nabla p + \frac{1}{\mathrm{Re}} \nabla^2 \mathbf{u}, \tag{3}$$

and the continuity constraint

$$\nabla \cdot \mathbf{u} = 0. \tag{4}$$

Using the identity $\mathbf{u} \cdot \nabla \mathbf{u} = \nabla(|\mathbf{u}|^2/2) - \mathbf{u} \times \boldsymbol{\omega}$, Eq. (3) is rewritten

$$\frac{\partial \mathbf{u}}{\partial t} = -\nabla P + \frac{1}{\mathrm{Re}} \nabla^2 \mathbf{u} + \mathbf{F}, \tag{5}$$

where $P \equiv p + |\mathbf{u}|^2/2$, and $\mathbf{F} \equiv \mathbf{u} \times \boldsymbol{\omega}$. Here, $\mathbf{u}$ is the velocity vector, $\boldsymbol{\omega} \equiv \nabla \times \mathbf{u}$ is the vorticity vector, and p is the kinematic pressure. The Navier–Stokes equation (3) is posed here as a nonlinearly forced Stokes problem.

In all spectral methods, the dependent variables are expressed in terms of a linear combination of known, smooth, global functions referred to as *basis functions*, while the momentum equation is satisfied in a weighted-residual or integral sense. Different choices of weight functions, referred to as *test functions*, correspond to different types of method (e.g., [12]). The first step of development consists in taking the dot product of Eq. (5) with specified test vector-functions $\mathbf{\Psi}_j$ and integrating over the whole domain, i.e.,

$$\left\langle \mathbf{\Psi}_j, \frac{\partial \mathbf{u}}{\partial t} \right\rangle = -\langle \mathbf{\Psi}_j, \nabla P \rangle + \frac{1}{\mathrm{Re}} \langle \mathbf{\Psi}_j, \nabla^2 \mathbf{u} \rangle + \langle \mathbf{\Psi}_j, \mathbf{F} \rangle \quad (6)$$

where $\langle \mathbf{a}, \mathbf{b} \rangle$ stands for the integral over the volume of the flow of the dot product of the vectors $\mathbf{a}$ and $\mathbf{b}$.

With the identity $\mathbf{\Psi}_j \cdot \nabla P = \nabla \cdot (P\mathbf{\Psi}_j) - P(\nabla \cdot \mathbf{\Psi}_j)$ and the divergence theorem, the first term on the right-hand side of Eq. (6) is now written as

$$\langle \mathbf{\Psi}_j, \nabla P \rangle = \int_S P(\mathbf{\Psi}_j \cdot \mathbf{n})\, dS - \int_V P(\nabla \cdot \mathbf{\Psi}_j)\, dV, \quad (7)$$

where V stands for the volume of the domain while S stands for its surface with unit, outward normal vector $\mathbf{n}$. This form makes it clear that *if* the test functions $\mathbf{\Psi}_j$ are divergence-free,

$$\nabla \cdot \mathbf{\Psi}_j = 0, \quad (8)$$

and if they satisfy the no-through flow condition on the solid boundaries, i.e.,

$$\mathbf{\Psi}_j \cdot \mathbf{n} = 0, \quad (9)$$

then $\langle \mathbf{\Psi}_j, \nabla P \rangle$ becomes identically zero.

This result is of fundamental importance in the present numerical method. Plainly, it says that if both conditions (8) and (9) are satisfied by an appropriate choice of the test functions, then the pressure term altogether "drops out." The resulting working equation therefore becomes

$$\left\langle \mathbf{\Psi}_j, \frac{\partial \mathbf{u}}{\partial t} \right\rangle = \frac{1}{\mathrm{Re}} \langle \mathbf{\Psi}_j, \nabla^2 \mathbf{u} \rangle + \langle \mathbf{\Psi}_j, \mathbf{F} \rangle, \quad (10)$$

where the multidimensional index j varies over the same index-space as the spectral expansions to be introduced in the next section.

4. VECTOR EXPANSIONS

In the method described in this paper, we follow Leonard and Wray [1] and represent the incompressible velocity field using divergence-free vector expansions which are made to satisfy all the boundary and geometry conditions: no-slip on the walls, periodicity in the ϕ-direction and regularity at the poles. This is accomplished first by decomposing the velocity field into two solenoidal components such that

$$\mathbf{u} = \mathbf{u}_h + \mathbf{u}_{bc} \quad (11)$$

where $\mathbf{u}_h$ is a contribution that satisfies homogeneous boundary conditions (zero velocity) on the $r = R_i$ and R_o walls, while $\mathbf{u}_{bc}$ is one that satisfies the actual boundary conditions on those walls. The latter can be viewed as a **known** divergence-free vector function easily constructed as shall be presented separately in Section 4.3. Therefore, one needs only focus at this stage on the construction of velocity expansions for $\mathbf{u}_h$ that span the whole homogeneous subspace of the divergence-free vector space in the spherical gap. Note that for brevity the subscript "h" is mostly omitted below.

In addition to the constraints already mentioned on our vector expansions, numerical efficiency requires that they also form complete sets as tightly "quasi-orthogonal" as possible. In all three-dimensional applications of the method so far, one has considered two periodic directions (purely orthogonal Fourier expansions) and one non-homogeneous direction (quasi-orthogonal expansions which yield banded topology for the uncoupled systems of discrete equations). For three-dimensional flows in spherical geometries, there are of course two non-periodic directions (r and θ). Stanaway *et al.* [10], who used a divergence-free expansion method to compute unbounded, spherically axisymmetric flows, have proposed in [13] that three-dimensional expansions based on vector spherical harmonics, VSH, may be employed effectively to alleviate the problem. We follow that lead in the construction of our own expansions below.

4.1. *Spherical Directions*

The directions θ and ϕ, taken together, define a two-dimensional surface corresponding to a spherical shell. On that surface, the family of three VSHs (see [11] and Appendix A) forms a complete set of orthonormal vector functions and can therefore be used to expand any arbitrary 3D vector field. In general,

$$\mathbf{u}(r, \theta, \phi, t) = \sum_{l=0}^{\infty} \sum_{m=-l}^{l} \begin{pmatrix} H^X_{lm}(r, t)\, \mathbf{X}_{l,m}(\theta, \phi) \\ + H^V_{lm}(r, t)\, \mathbf{V}_{l,m}(\theta, \phi) \\ + H^W_{lm}(r, t)\, \mathbf{W}_{l,m}(\theta, \phi) \end{pmatrix}, \quad (12)$$

where $\mathbf{X}_{l,m}$, $\mathbf{V}_{l,m}$, and $\mathbf{W}_{l,m}$ are the three independent vector harmonics which satisfy the orthogonality relation

$$\int_0^{2\pi} \int_0^{\pi} \mathbf{C}_{lm} \cdot [\mathbf{D}_{l'm'}]^* \sin\theta\, d\theta\, d\phi = \delta_{\mathbf{CD}} \delta_{ll'} \delta_{mm'}, \quad (13)$$

where * denotes the complex conjugate, and the vectors **C** and **D** are any of $\mathbf{X}_{l,m}$, $\mathbf{V}_{l,m}$, or $\mathbf{W}_{l,m}$. Using Eq. (13), one easily obtains explicit expressions for any of the complex-valued coefficient functions in (12), for example,

$$H^X_{lm}(r, t) = \int_0^{2\pi} \int_0^{\pi} \mathbf{u}(r, \theta, \phi, t) \cdot \mathbf{X}^*_{l,m}(\theta, \phi) \sin\theta \, d\theta \, d\phi. \quad (14)$$

It can be shown that the truncated version of expansion (12) exhibits spectral convergence as long as the vector field is infinitely differentiable. In addition to this spectral behavior and the crucial orthogonality in both θ and ϕ, the VSHs offer uniform resolution over the whole spherical surface, thus avoiding the stringent timestepping stability limit associated with the azimuthal clustering of the collocation grid near the poles [14]. Some fundamental results and useful properties of the VSHs, and of the SSHs (scalar spherical harmonics) from which they are built, are provided in Appendix A.

A divergence-free vector field can be represented using only two independent sets of basis vectors as

$$\mathbf{u}(r, \theta, \phi, t) = \sum_{l=0}^{L} \sum_{m=-l}^{l} \left\{ \begin{matrix} H^-_{lm}(r, t)\, \mathbf{X}_{l,m}(\theta, \phi) + \\ \nabla \times [H^+_{lm}(r, t)\, \mathbf{X}_{l,m}(\theta, \phi)] \end{matrix} \right\}, \quad (15)$$

where a finite truncation "L" has been introduced. Equation (15) is simply the divergence-free subspace version of the general expansion (12). Using the result (A.17), one obtains the following relations between the H_{lm} functions of those two expansions:

$$\begin{aligned} H^X_{lm}(r, t) &= H^-_{lm}(r, t) \\ H^V_{lm}(r, t) &= i\left(\frac{l}{2l+1}\right)^{1/2} \left[\frac{\partial H^+_{lm}(r, t)}{\partial r} - \frac{l}{r} H^+_{lm}(r, t)\right] \\ H^W_{lm}(r, t) &= i\left(\frac{l+1}{2l+1}\right)^{1/2} \left[\frac{\partial H^+_{lm}(r, t)}{\partial r} + \frac{l+1}{r} H^+_{lm}(r, t)\right]. \end{aligned} \quad (16)$$

Leaving the radial functions arbitrary for now in a discrete space truncated at "N," the time and radial dependences are separated as

$$\begin{aligned} H^-_{lm}(r, t) &= \sum_{n=0}^{N} a^-_{nlm}(t) \;\; h^-_n(r) \\ H^+_{lm}(r, t) &= \sum_{n=0}^{N} a^+_{nlm}(t) \;\; h^+_n(r). \end{aligned} \quad (17)$$

No index l nor m is needed for the $h^{\pm}$ functions above due to their common homogeneous boundary conditions, i.e., each of the radial functions in a given class must lead to the same zero end-conditions irrespective of l and m. In terms of the general expansion (12), one thus has

$$\begin{aligned} H^V_{lm}(r, t) &= \sum_{n=0}^{N} a^+_{nlm}(t) \;\; h^{+V}_{nl}(r) \\ H^W_{lm}(r, t) &= \sum_{n=0}^{N} a^+_{nlm}(t) \;\; h^{+W}_{nl}(r), \end{aligned} \quad (18)$$

where, from (16),

$$\begin{aligned} h^{+V}_{nl}(r) &= i\left(\frac{l}{2l+1}\right)^{1/2} \left[\frac{dh^+_n}{dr} - \frac{l}{r} h^+_n\right] \\ h^{+W}_{nl}(r) &= i\left(\frac{l+1}{2l+1}\right)^{1/2} \left[\frac{dh^+_n}{dr} + \frac{l+1}{r} h^+_n\right]. \end{aligned} \quad (19)$$

For the time-independent test functions, one similarly chooses two distinct classes of vectors that together span the whole divergence-free space on a sphere of radius r (thus satisfying exactly constraint (8), the first fundamental condition on $\mathbf{\Psi}_j$), i.e.,

$$\begin{aligned} \mathbf{\Psi}^-_{n'l'm'}(r, \theta, \phi) &= g^-_{n'}(r)\, \mathbf{X}^*_{l',m'}(\theta, \phi) \\ \mathbf{\Psi}^+_{n'l'm'}(r, \theta, \phi) &= \nabla \times [g^+_{n'}(r)\, \mathbf{X}^*_{l',m'}(\theta, \phi)] \end{aligned} \quad (20)$$

where $0 \leqslant n' \leqslant N$, $0 \leqslant l' \leqslant L$, and $|m'| \leqslant l'$. Here, the complex conjugate of $\mathbf{X}_{l,m}$ is introduced purely for convenience. Using again Eq. (A.17), the "$+$" class of test functions is rewritten as

$$\mathbf{\Psi}^+_{n'l'm'} = g^{+V}_{n'l'}(r)\, \mathbf{V}^*_{l',m'}(\theta, \phi) + g^{+W}_{n'l'}(r)\, \mathbf{W}^*_{l',m'}(\theta, \phi), \quad (21)$$

where

$$\begin{aligned} g^{+V}_{n'l'}(r) &= -i\left(\frac{l'}{2l'+1}\right)^{1/2} \left[\frac{dg^+_{n'}}{dr} - \frac{l'}{r} g^+_{n'}\right] \\ g^{+W}_{n'l'}(r) &= -i\left(\frac{l'+1}{2l'+1}\right)^{1/2} \left[\frac{dg^+_{n'}}{dr} + \frac{l'+1}{r} g^+_{n'}\right]. \end{aligned} \quad (22)$$

One now proceeds to evaluate the spherical contributions in the integrals forming the weighted-residual equation (10). The task is made quite simple by the uncoupling of the $^-$ and $^+$ classes of functions due to the orthogonality property (14) and by the simple relations of (A.18) for the Laplacian operator. Substituting in the velocity expansion (15) and each of the functions (20) and (21) for $\mathbf{\Psi}_j$, one obtains for every modal pair (l, m) two uncoupled systems of "$N+1$" ODEs for the unknown coefficients $a^{\pm}_{nlm}$:

$$\sum_{n=0}^{N}\left\{\frac{da_{nlm}^{-}}{dt}\int_{R_i}^{R_o} h_n^{-}\, g_{n'}^{-}\, r^2\, dr - \frac{1}{\mathrm{Re}}\, a_{nlm}^{-}\int_{R_i}^{R_o}\mathscr{L}_l(h_n^{-})\, g_{n'}^{-}\, r^2\, dr\right\} = \int_{R_i}^{R_o} f^{X}(r)\, g_{n'}^{-}\, r^2\, dr \tag{23}$$

for the $^-$ class, and

$$\sum_{n=0}^{N}\left\{\frac{da_{nlm}^{+}}{dt}\int_{R_i}^{R_o}(h_{nl}^{+V}\, g_{n'l}^{+V} + h_{nl}^{+W}\, g_{n'l}^{+W})\, r^2\, dr - \frac{1}{\mathrm{Re}}\, a_{nlm}^{+}\int_{R_i}^{R_o}[\mathscr{L}_{l+1}(h_{nl}^{+V})\, g_{n'l}^{+V} + \mathscr{L}_{l-1}(h_{nl}^{+W})\, g_{n'l}^{+W}]\, r^2\, dr\right\} = \int_{R_i}^{R_o}[f^{V}(r)\, g_{n'l}^{+V} + f^{W}(r)\, g_{n'l}^{+W}]\, r^2\, dr \tag{24}$$

for the $^+$ class. In these relations, the index n' takes all integer values on $[0, N]$, and the scalar differential operator $\mathscr{L}_l$ is defined in (A.19) as $d^2/dr^2 + (2/r)(d/dr) - l(l+1)/r^2$. The radial functions $f^{X,V,W}(r)$ are respectively the **X**, **V** and **W** components of the VSH transform (discussed in Section 5) of the nonlinear forcing vector $\mathbf{F} \equiv \mathbf{u}\times\boldsymbol{\omega} = (\mathbf{u}_h + \mathbf{u}_{bc})\times(\boldsymbol{\omega}_h + \boldsymbol{\omega}_{bc})$.

4.2. *Radial Direction*

The finite dimensionless interval $R_i \leqslant r \leqslant R_o$ is first mapped into the standard domain $-1 \leqslant \xi \leqslant 1$ by $\xi(r) = 2r - K$, where the new geometric parameter K, redundant with δ but nonetheless useful, is given by $K \equiv (2+\delta)/\delta = R_i + R_o$. Chebyshev polynomials $T_n(\xi)$ are then chosen to construct the radial functions. They are defined within the interval $-1 \leqslant \xi \leqslant 1$ on which they satisfy the orthogonality relation

$$\int_{-1}^{1}\omega(\xi)\, T_n(\xi)\, T_m(\xi)\, d\xi = \frac{\pi}{2}\, c_n \delta_{nm}, \tag{25}$$

where $\omega(\xi) = (1-\xi^2)^{-1/2}$ is the weight function, $c_0 = 2$, and $c_n = 1$ for $n > 0$.

Using the results of Appendix A and the velocity expansions defined by (12) and (15) to (19), it is easy to verify that the radial basis functions $h_n^{-}(r)$ and $h_n^{+}(r)$ must satisfy the following end-conditions in order to enforce the homogeneous, no-slip boundary conditions, i.e., $\mathbf{u}(r = R_i) = \mathbf{u}(r = R_o) = \mathbf{0}$:

$$\begin{aligned} h_n^{-}(R_i) &= h_n^{-}(R_o) = 0, \\ h_n^{+}(R_i) &= h_n^{+}(R_o) = \frac{d}{dr}h_n^{+}(R_i) = \frac{d}{dr}h_n^{+}(R_o) = 0. \end{aligned} \tag{26}$$

The question of end-conditions for the radial test functions $g_{n'}^{-}(r)$ and $g_{n'}^{+}(r)$, introduced in (20) to (22), is somewhat more delicate. This is due to the necessary inclusion of the singular Chebyshev weight function $\omega(\xi) = (1-\xi^2)^{-1/2}$ within the test functions in order to take advantage of the orthogonality property (25) in the evaluation of the weighted residual integrals (23) and (24).

The basic condition (9) on the test vector-space states that it must (at least) satisfy the "no-through flow" condition. A more precise definition of the space is, however, available from the theoretical analysis of Pasquarelli *et al.* [16] who studied Leonard and Wray's method applied in conjunction with Chebyshev polynomials. By considering the numerical procedure as being a projection method with respect to the Chebyshev-weighted L_ω^2 inner-product space, they have specialized the projection argument of Moser and Moin [8] and have shown that, in addition to conditions (8) and (9) on $\boldsymbol{\Psi}_j$, the vector space "$\boldsymbol{\Psi}_j/\omega$" should also satisfy the no-slip condition (similarly to the basis vector space), i.e.,

$$\boldsymbol{\Psi}_j/\omega\Big|_{r = R_i, R_o} = \mathbf{0}. \tag{27}$$

The proofs of stability and convergence given by Pasquarelli *et al.* are important contributions in that they have provided the additional and formal support required to complement the prior evidence from numerical experiments [17].

Applying condition (27) on the test vectors given by (20) to (22), yields similar boundary conditions for the test functions "$g^{\pm}/\omega$" as the ones written in (26) for the basis functions. We are thus specifically interested here in *single-zero* and *double-zero* radial spaces. Such subspaces can be formed systematically by a *space restrictor approach*, i.e.,

$$\{\text{subspace set}\} = \{\text{space restrictor}\} \times \{\text{general set}\},$$

where the product of the space restrictor with the general set must lead to a polynomial representation. One must therefore choose a polynomial function for the space restrictor. It is no challenge to convince oneself that $(1-\xi^2)$ for the single-zero restrictor, and $(1-\xi^2)^2$ for the double-zero restrictor, are the lowest order polynomials to enforce exactly the appropriate restrictions. The interested reader may consult [18] for an alternative, more general method of generating any subspaces (the *linear combination approach*). Our radial basis functions are thus constructed here as

$$\begin{aligned} h_n^{-}(r(\xi)) &= (1-\xi^2)\, T_n(\xi) \\ h_n^{+}(r(\xi)) &= (1-\xi^2)^2\, r\; T_n(\xi), \end{aligned} \tag{28}$$

from which, by Eq. (19), the $^+$ class decomposes as

$$\begin{aligned} h_{nl}^{+V}(r) &= i\left(\frac{l}{2l+1}\right)^{1/2}\begin{Bmatrix}(1-l)\;[(1-\xi^2)^2\;\; T_n(\xi)] + \\ (\xi+K)\;[(1-\xi^2)^2\, T_n(\xi)]'\end{Bmatrix} \\ h_{nl}^{+W}(r) &= i\left(\frac{l+1}{2l+1}\right)^{1/2}\begin{Bmatrix}(2+l)\;[(1-\xi^2)^2\;\; T_n(\xi)] + \\ (\xi+K)\;[(1-\xi^2)^2\, T_n(\xi)]'\end{Bmatrix}, \end{aligned} \tag{29}$$

where the superscript ′ on bracketed terms indicates derivative with respect to ξ. Note that the presence of the factor r in the h_n^+ function is necessary to yield an exact polynomial representation for the radial expansions in (29).

The radial test functions, which must include the Chebyshev weight function, are obtained similarly, i.e.,

$$\begin{aligned} g_{n'}^-(r(\xi)) &= \frac{1}{(1-\xi^2)^{1/2}}(1-\xi^2)\,T_{n'}(\xi) \\ g_{n'}^+(r(\xi)) &= \frac{1}{(1-\xi^2)^{1/2}}(1-\xi^2)^2\, r\;T_{n'}(\xi). \end{aligned} \tag{30}$$

For the $^+$ class, this translates by Eq. (22) into

$$\begin{aligned} g_{n'l}^{+V}(r) &= -i\left(\frac{l}{2l+1}\right)^{1/2}\frac{1}{(1-\xi^2)^{1/2}} \\ &\quad\times\left\{\begin{array}{l}(1-l)\;[(1-\xi^2)^2\;\;T_{n'}(\xi)] \\ +\xi(\xi+K)\;[(1-\xi^2)\,T_{n'}(\xi)] \\ +(\xi+K)\;[(1-\xi^2)^2\,T_{n'}(\xi)]'\end{array}\right\} \\ g_{n'l}^{+W}(r) &= -i\left(\frac{l+1}{2l+1}\right)^{1/2}\frac{1}{(1-\xi^2)^{1/2}} \\ &\quad\times\left\{\begin{array}{l}(l+2)\;[(1-\xi^2)^2\;\;T_{n'}(\xi)] \\ +\xi(\xi+K)\;[(1-\xi^2)\,T_{n'}(\xi)] \\ +(\xi+K)\;[(1-\xi^2)^2\,T_{n'}(\xi)]'\end{array}\right\}. \end{aligned} \tag{31}$$

It can be verified that both the basis and the test functions above form complete sets of quasi-orthogonal functions in the appropriate subspaces. Indeed, through extensive use of the Chebyshev orthogonality property, they permit a straightforward evaluation of the weighted-residual integrals (23) and (24). This results in non-symmetrical matrices with regular and thinly banded topologies. Those matrices are synthesized in Appendix B and can be easily constructed. The half-bandwidths of the inertia matrices $\mathscr{A}^-$ and $\mathscr{A}^+$ are 6 and 10 while those of the viscous matrices $\mathscr{B}^-$ and $\mathscr{B}^+$ are 4 and 8.

4.3. *Boundary-Condition Terms*

In this section, the boundary condition part of the velocity decomposition (11) is chosen, and its contribution to the weighted-residual equation (10) is discussed. It is recalled that $\mathbf{u}_{bc}$ must be a divergence-free vector field that satisfies the solid-body rotation conditions on the two walls, i.e., Eq. (1).

It can be verified (e.g., Appendix B of [11]) that the vector spherical harmonic $\mathbf{X}_{l,m}$, with $l=1$ and $|m|\leqslant 1$, provides exactly the right θ-ϕ functional form to describe solid-body rotation of spherical shells with respect to arbitrary axis, i.e.,

$$\begin{aligned} \mathbf{u}_{\text{solid}}(\theta,\phi) &= (K_1\sin\phi)\,\hat{\mathbf{e}}_\theta\;+ \\ &\quad (K_2\sin\theta + K_1\cos\theta\cos\phi)\,\hat{\mathbf{e}}_\phi, \end{aligned} \tag{32}$$

where K_1 and K_2 are constants. Therefore, it only remains to choose a radial function to build the $\mathbf{u}_{bc}$ field. The simplest and most convenient choice is clearly a linear variation. One thus writes

$$\mathbf{u}_{bc}(r(\xi),\theta,\phi) = \sum_{m=-1}^{1}\Big[C_m(1-\xi)+D_m(1+\xi)\Big]\mathbf{X}_{1,m}(\theta,\phi). \tag{33}$$

Introducing the actual (possibly time-dependent) boundary conditions (1) and expressing the result in terms of Chebyshev polynomials, one obtains the desired non-homogeneous velocity expansion

$$\mathbf{u}_{bc}(r(\xi),\theta,\phi,t) = \sum_{m=-1}^{1}\Big[\Lambda_m^0(t)\,T_0(\xi)+\Lambda_m^1(t)\,T_1(\xi)\Big]\mathbf{X}_{1,m}(\theta,\phi), \tag{34}$$

where the known, dimensionless boundary parameters are given by

$$\begin{aligned} \Lambda_0^0(t) &= -i\left(\frac{2\pi}{3}\right)^{1/2}\left[V_o(t)\cos\Big(\alpha_o(t)\Big)+V_i(t)\right] \\ \Lambda_0^1(t) &= -i\left(\frac{2\pi}{3}\right)^{1/2}\left[V_o(t)\cos\Big(\alpha_o(t)\Big)-V_i(t)\right] \\ \Lambda_{\pm1}^{0,1}(t) &= \pm i\left(\frac{\pi}{3}\right)^{1/2}V_o(t)\sin\Big(\alpha_o(t)\Big). \end{aligned} \tag{35}$$

The contribution of the non-homogeneous field into the weighted-residual equation is now easily determined. Thanks to the VSH orthogonality property, the only non-zero contributions come from the dot products with the $^-$ class of test functions (20) when $l=1$. One finds for the inertia and the viscous term respectively

$$\begin{aligned} \Big\{T^{bc}(t)\Big\}_m &= \int_{R_i}^{R_o}\Big[\dot{\Lambda}_m^0(t)\,T_0(\xi)+\dot{\Lambda}_m^1(t)\,T_1(\xi)\Big]\,g_{n'}^-(r)\,r^2\,dr, \\ \Big\{V^{bc}(t)\Big\}_m &= 2\Big[K\Lambda_m^1(t)-\Lambda_m^0(t)\Big]\int_{R_i}^{R_o} g_{n'}^-(r)\,dr, \end{aligned} \tag{36}$$

where the dot superscript indicates derivative with respect to time. In the above results, m takes the three values -1, 0, and 1, n' ranges from 0 to N, and T_0 and T_1 are respectively the zeroth and first-degree Chebyshev polynomials ($T_0=1$, $T_1=\xi$). Using again the Chebyshev orthogonality property (25), it is straightforward to evaluate those radial integrals and thus to construct the necessary T_m^{bc} and V_m^{bc} one-dimensional arrays of size $N+1$ (in which most of the components are zero). These arrays are then added appropriately to the "$l=1$" system of ODEs of the $^-$ class.

A convenient summary of the present spatial discretization, including the complete expression for the velocity expansion and the matrix form of the semi-discrete systems of equations, is presented in Appendix B.

5. IMPLEMENTATION

5.1. *Time-Integration*

Simple, standard time-marching procedures can be used to integrate the systems of ODEs for the unknown expansion coefficients. The classical algorithm adopted here consists of a mixed (explicit–implicit) finite-difference-type method. The viscous term is treated implicitly by the second-order Crank–Nicolson scheme. Since inversion of the inertia matrix $\mathscr{A}$ in Eq. (B.2) is clearly unavoidable, and since $\mathscr{A}$ has a larger bandwidth than $\mathscr{B}$, the implicit treatment of the viscous term comes at no extra cost.

The remaining terms, the nonlinear convection and the boundary-condition terms, are all integrated by the explicit, single-step, second-order Adams–Bashforth scheme. For each pair (l, m), the systems of ODEs (B.2) thus become the discrete systems written symbolically as

$$\left[\mathscr{A}^{\pm} - \frac{\Delta t}{2\mathrm{Re}}\mathscr{B}^{\pm}\right]\left\{a_n^{\pm}\right\}^{j+1} = \left[\mathscr{A}^{\pm} + \frac{\Delta t}{2\,\mathrm{Re}}\mathscr{B}^{\pm}\right]\left\{a_n^{\pm}\right\}^{j} + \frac{3\Delta t}{2}\left\{\mathscr{R}^{\pm}\right\}^{j} - \frac{\Delta t}{2}\left\{\mathscr{R}^{\pm}\right\}^{j-1} \tag{37}$$

with the superscript j as index for the timesteps, and

$$\mathscr{R}^{+} \equiv \mathscr{F}^{+}, \qquad \mathscr{R}^{-} \equiv \mathscr{F}^{-} - T^{bc^{-}}\delta_{l,1} + \frac{1}{\mathrm{Re}}V^{bc^{-}}\delta_{l,1}. \tag{38}$$

This time-integration scheme is globally second-order accurate and conditionally stable. A CFL number of 0.50 to 0.70, based on local velocities and the transform collocation grid, ensured numerical stability and accuracy. It is important to note that the actual clustering of the azimuthal collocation points towards the poles ($\Delta\phi \sim \sin\theta$) does not have to be taken into account in the CFL definition due to the uniform resolution of the spherical harmonics over the whole sphere [18]. This property allows for reasonable timestep sizes to be used and represents a fundamental advantage of the VSHs over alternative choices of expansions [14].

The matrices involved in the discrete systems (37) are all real and independent of the index m. For a given l, the band-structured equations are constructed from pre-computed (l-independent) basic matrices and are solved by classical Gauss elimination with up to $M+1$ complex, m-dependent right-hand sides where $M \leqslant l$ (see [18]). Furthermore, only the spectral coefficients with $m \geqslant 0$ are actually integrated in time. The remaining coefficients are automatically determined with $a^{\pm}_{n,l,-m} = (-1)^{m+1}\,[a^{\pm}_{n,l,m}]^{*}$ which must hold due to the indicial symmetries of the VSHs and the reality of the velocity field $\mathbf{u}$.

5.2. *Discrete Transforms*

As presented so far, the complete set of VSHs up to *degree* L ($0 \leqslant |m| \leqslant l \leqslant L$) has been considered. However, one can restrict the maximum *order* of the VSH expansions to a smaller value than L, say M, such as in the case of axisymmetric flows where $M \equiv 0$. In general, one thus implements the velocity expansion (B.1) as

$$\mathbf{u} = \sum_{n=0}^{N}\sum_{m=-M}^{M}\sum_{l=|m|}^{L}\left\{\begin{matrix} a^{-}_{nlm}\; h_n^{-}\mathbf{X}_{l,m} + \\ a^{+}_{nlm}\nabla\times[h_n^{+}\mathbf{X}_{l,m}]\end{matrix}\right\} + \sum_{m=-1}^{1}[\Lambda_m^0 T_0 + \Lambda_m^1 T_1]\,\mathbf{X}_{1,m}, \tag{39}$$

where $M \leqslant L$. That form makes it clear that the three truncation parameters N, M, and L can be chosen separately and optimally to achieve a desired level of resolution.

The efficient implementation of the present numerical method requires back and forth transforms of the unknowns between spectral and physical spaces (see Section 5.3). This capability rests upon the existence of a discrete VSH–Chebyshev transform associated with the standardized, *generic VSH–Chebyshev expansion*

$$\mathbf{u}\left(r(\xi),\theta,\phi\right) = \sum_{n=0}^{N_d} T_n(\xi)\sum_{m=-M_d}^{M_d} e^{im\phi}\sum_{l=|m|}^{L_d}\left(\begin{matrix} A_{nlm}\mathbf{X}_{l,m}(\theta) = \\ + B_{nlm}\mathbf{V}_{l,m}(\theta) \\ + C_{nlm}\mathbf{W}_{l,m}(\theta)\end{matrix}\right) \tag{40}$$

in which the $\theta-\phi$ functional contributions of the VSHs have been separated thanks to (A.12): the *polar vectors* $\mathbf{X}_{l,m}(\theta)$, $\mathbf{V}_{l,m}(\theta)$ and $\mathbf{W}_{l,m}(\theta)$ (defined in Appendix A) for the polar variable θ, and the Fourier complex exponential $e^{im\phi}$ for the azimuthal variable ϕ. Recall that the restriction $M_d \leqslant L_d$ always applies. It is thus clear that the three-dimensional vector transform corresponding to (40) can be performed as a sequence of one-dimensional transforms where only the polar direction involves vector functions. Standard Fourier transforms of size $2M_d+2$ and standard Chebyshev transforms of size N_d are used in the azimuthal and radial direction, respectively. Both of these are fast algorithms implemented with FFTs on the collocation grids given by $\phi_j = j\pi/(M_d+1)$ for $j = 0, 1, \ldots, 2M_d+1$ in the

azimuthal direction, and $\xi_j = \cos(j\pi/N_d)$ for $j = 0, 1, ..., N_d$ in the mapped radial direction.

It is shown in [18] that, for the polar direction, a discrete backward transform based on Gauss–Legendre quadrature can be developed and be exact in the discrete space despite the polar vectors not being, in general, polynomials themselves. The $L_d + 2$ collocation points used correspond to the zeroes of the Legendre polynomial $P_{L_d+2}(\mu)$ with $\mu_j = \cos\theta_j$ and are almost uniformly distributed along the polar domain $0 < \theta < \pi$. The polar vectors transforms (backward and forward) are thus "slow transforms" ($O(L_d^2)$ operations) yielding a total operation-count for the whole VSH-Chebyshev transforms that scales as $O\{N_d L_d M_d [L_d + 2\log(M_d N_d)]\}$. To achieve full vectorization of the transforms in the polar direction, it is necessary to pre-compute the polar vectors $\boldsymbol{X}_{l,m}$, $\boldsymbol{V}_{l,m}$, and $\boldsymbol{W}_{l,m}$ (total of eight components computed from associated Legendre functions by standard recurrence routines) at the θ_j collocation points, thus requiring $4(L_d+2)(M_d+1)(2L_d - M_d + 2)$ real words of memory e.g., $L_d = 129$ and $M_d = 31 \rightarrow 3.8$ MWords.

5.3. *Nonlinear Terms and Aliasing*

The nonlinear terms $\mathscr{F}^{\pm}$ in the discrete systems (B.2) result from the inner products $\langle \boldsymbol{\Psi}_j, \mathbf{u} \times \boldsymbol{\omega} \rangle$. Their computations use a standard collocation approach, i.e., the product $\mathbf{F} \equiv \mathbf{u} \times \boldsymbol{\omega}$ is handled in physical space rather than through a convolution sum in spectral space. At each timestep, generic VSH–Chebyshev representations (e.g., Eq. (40) for the velocity) of both the velocity and the vorticity vectors are obtained from the basic velocity expansion (39). Using common properties of the VSH and Chebyshev polynomials, this first step is efficiently implemented through multiplications of real, pre-computed, banded matrices by complex vectors. The generic expansion coefficients of both vector fields are then forward transformed into physical space where the vector product is computed at each node of the collocation grid. For convenience, one computes the product "$r(\mathbf{u} \times r\boldsymbol{\omega})$" rather than simply $\mathbf{F}$. By a backward transform of the resulting vector field, one obtains the expansion coefficients corresponding to the generic VSH–Chebyshev representation of the nonlinear product. The final step involves again banded matrix–vector multiplications for the evaluation of radial integrals and produces the desired nonlinear terms $\mathscr{F}^{\pm}$.

It can be shown that the inner product $\langle \boldsymbol{\Psi}_j, \mathbf{u} \times \boldsymbol{\omega} \rangle$ is evaluated exactly, i.e., without aliasing error, if the truncation limits M_d, L_d, and N_d are set according to the so-called "3/2-rule" [18]:

$$\begin{aligned} N_d &= \tfrac{3}{2}(N+4)+1 \\ M_d &= \tfrac{3}{2}M+1 \\ L_d &= \tfrac{3}{2}(L+1)+1. \end{aligned} \tag{41}$$

For all the numerical simulations in this study, the above *collocation truncations* are used. The method can thus be said to be totally de-aliased in the discrete VSH–Chebyshev space truncated at M, L, and $N+4$.

6. NUMERICAL TESTS

This section presents a few of the tests performed in order to validate the spectral code which implements the numerical approach described in the previous sections. One may refer to the thesis by Dumas [18] for a complete and more detailed exposition.

We restrict the present discussion to test problems belonging to the general category of "spherical Couette flows" with steady-state boundary conditions and with both axes of rotation aligned with the vertical z-direction ($\alpha_o = 0$). We further restrict the presentation to cases for which either the inner or the outer sphere is held stationary. The number of relevant parameters thus reduces to only two: the gap-width ratio ($\delta \equiv \bar{d}/\bar{R}_i = 1/R_i$) and the Reynolds number ($\mathrm{Re} \equiv \bar{V}\bar{d}/\nu$, where $\bar{V} = \bar{V}_i$ or $\bar{V}_o$). Both axisymmetric and fully three-dimensional flows are computed and are compared with existing experimental and numerical results.

6.1. *Axisymmetric Flows*

Basic spherical Couette flows are axisymmetric and in the limit $\mathrm{Re} \rightarrow 0$, the Stokes solution is known as

$$\mathbf{u}_{\mathrm{Stokes}} = \left(\alpha r + \frac{\beta}{r^2}\right) \sin\theta \ \hat{\mathbf{e}}_{\phi}, \tag{42}$$

where α and β are constants that depend on the boundary conditions and the gap size. This solution is obviously axisymmetric and exclusively azimuthal in direction (no meridional velocity, i.e., $\mathbf{u}_m = \mathbf{0}$). The corresponding angular velocity ($\Omega = u_\phi / r \sin\theta$) is not a function of θ so that the iso-Ω contours are all concentric spherical shells.

For any non-vanishing Re, however, nonlinear effects always lead to the generation of a meridional circulation. This can be verified by a simple analysis of the nonlinear interaction of the Stokes flow with itself (e.g., [22]) in accordance with the Ekman pumping phenomenon taking place near the rotating surface in the pole region. The laminar, subcritical regime in spherical Couette flow is thus the combination of a primary azimuthal motion and a secondary meridional circulation which strongly depends on Re and δ (e.g., [5]).

We consider first the basic steady-state flow in a large-gap geometry $\delta = 1.0$ ($R_i = 1$, $R_o = 2$) with a stationary inner sphere and a rotating outer shell. The truncation limits are set to $N = 16$, $L = 42$, and $M = 0$, yielding a timing of 0.22

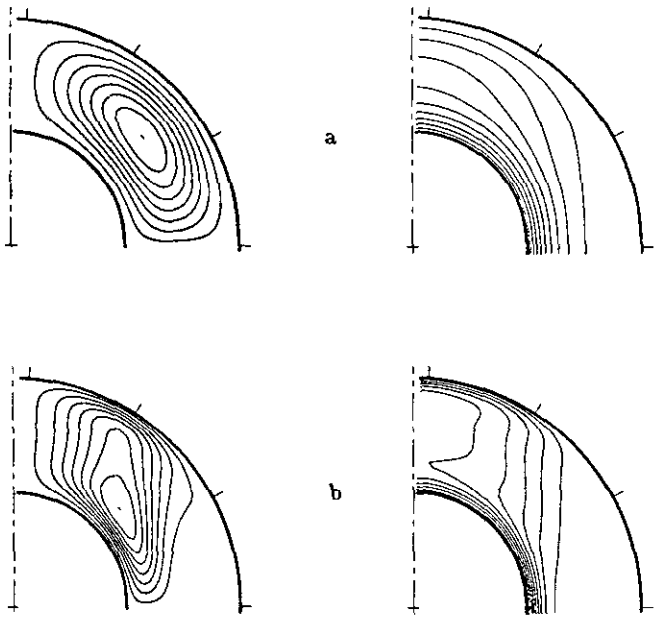

FIG. 2. Meridional streamlines Ψ and angular velocity contours Ω of the steady-state axisymmetric solutions at $\mathrm{Re} = \bar{V}_o \bar{d}/\nu$ (a) 50 ($\Psi_{\max} = 0.0144$), and (b) 500 ($\Psi_{\max} = 0.00737$) with $\delta = 1.0$, $V_i = 0$, and $V_0 = 1$. Solutions are reflection-symmetric about the equator. The circumferential distance between the tick marks on the outer sphere corresponds to the gap-width d.

CPU-s/timestep on a single processor of the CRAY Y/MP. Several Reynolds number flows from zero to 500 have been computed. Figure 2 shows two such computed flow fields by means of contour-plots of the meridional streamfunction Ψ ($\mathbf{u}_m = \nabla \times [(\Psi/r \sin\theta)\,\hat{\mathbf{e}}_\phi]$) and the angular velocity Ω. The solution being (freely) reflection-symmetric about the equator, only the upper half of the domain is shown.

It is observed that even at a Reynolds number as low as 50, the meridional recirculation (positive and therefore clockwise in the upper hemisphere) has developed strongly enough to significantly affect the distribution of angular momentum between the spheres, as shown by Fig. 2a, where the departure from the Stokes solution is clearly visible. With increasing Re, the secondary flow intensity increases and the center of the recirculation cell moves closer to the inner sphere while confining itself within a cylindrical envelope of radius approaching R_i. Outside that envelope, there exists a region of essentially constant angular velocity ($\simeq \Omega_o$) as well as a very weak counter-circulation cell near the equator (not visible, however, on the constant-increment Ψ-contours of Fig. 2b).

TABLE I

Comparison of Dimensionless Torque Υ

Investigator	Torque Υ
Present	16.702
Gagliardi *et al.* [30]	16.29
Yang [28]	16.72
Dennis and Quartapelle [27]	16.99
Dennis and Singh [31]	16.76
Munson and Joseph [24]	16.65

Note. $\mathrm{Re} = 50$, $\delta = 1.0$, $V_i = 0$, $V_o = 1$.

Over the past two decades, a number of researchers have reported numerical results for that same problem using either finite difference or perturbation methods which explicitly assumed axisymmetry as well as reflection-symmetry about the equator [23–30]. A comparison of our flow solutions (e.g., location and magnitude of $\Psi_{\max}$) with the ensemble of those results showed good agreement as detailed in [18]. Table I provides a quantitative comparison for $\mathrm{Re} = 50$ of the steady-state dimensionless torque Υ as given by

$$\Upsilon \equiv \frac{\bar{\tau}}{\bar{\rho}\bar{\nu}\bar{V}_{ref}\bar{d}^2} = -2\pi r^3 \int_{-1}^{1} \sin\theta \left[\frac{\partial u_\phi}{\partial r} - \frac{u_\phi}{r}\right] d\mu \quad (43)$$

with $\mu \equiv \cos\theta$, and where the integral is evaluated at $r = R_i$ to get the inner torque Υ_i or at $r = R_o$ for the outer torque Υ_o, both of which being equal for truly steady-state solutions. For our computations, the time integration was pursued until the relative difference between the two was less than 10^{-5}. We believe that our result is accurate to the five digits shown. Other investigators' results have been appropriately standardized according to (43) and are given here with the provided accuracy. Furthermore, when both inner and outer torques were available (and found different), the average torque was selected. We add for reference two more of our computed results: $\Upsilon(\mathrm{Stokes}) = 14.362$ and $\Upsilon(\mathrm{Re} = 500) = 28.896$.

Our second set of benchmark cases consists in spherical Couette flows occurring in a moderate gap $\delta = 0.18$ with a rotating inner sphere and a stationary outer shell ($V_i = 1$, $V_o = 0$). An abundant experimental, theoretical, and numerical literature exists on this basic flow and its axisymmetric transition states which are often referred to as "spherical Taylor–Couette flows" (e.g., [3, 7, 32, 33]). In a significant two-part paper [6], Marcus and Tuckerman have described and used an axisymmetric, pseudospectral method for the study of those flows. With our spectral code, two of their high-resolution simulations (16 Chebyshev × 128 sine functions) have been very well reproduced with similar truncations: (1) a steady-state, subcritical *zero-vortex flow with pinches*, and (2) a time-evolving flow corresponding to the so-called $0 \to 2$ *transition*. Results for the former are discussed below while the latter are presented in [18] and are used in [22] for a discussion on the transition mechanism involved which is shown to be a deterministic process independent of a centrifugal instability.

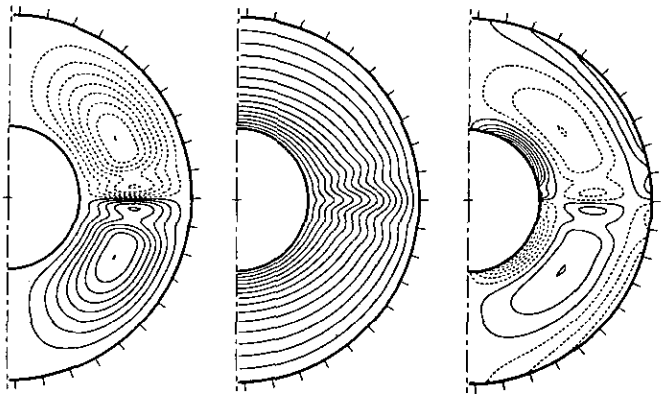

FIG. 3. Steady-state axisymmetric solution at $\mathrm{Re} = \bar{V}_i \bar{d}/\nu = 117$ for $\delta = 0.18$, $V_i = 1$, and $V_o = 0$. Shown from left to right are the contours of the streamfunction Ψ, the angular velocity Ω, and the azimuthal vorticity ω_ϕ. For clarity, the radial direction on the contour plots has been amplified four times. Full and dashed lines represent respectively positive and negative contour values.

Using the truncations $N = 16$ and $L = 84$ ($N_d = 32$, $L_d = 129$), the steady axisymmetric flow at $\mathrm{Re} = 117$, i.e., just below the critical value for the onset of Taylor vortices, was computed. Figure 3 and Fig. 4 show respectively the flow field via contours of Ψ, Ω, and ω_ϕ (azimuthal vorticity component), and the energy spectra $E_\phi(l)$ and $E_m(l)$. Both figures can be compared directly with Figs. 7 to 9 of Marcus and Tuckerman [6]. The energy spectra of Fig. 4 are easily computed from the definition of the total kinetic energy of the flow per unit volume, i.e., $E = (1/2v)\int_v \mathbf{u}\cdot\mathbf{u}^*\, dv$, where $v \equiv 4\pi(R_o^3 - R_i^3)/3$ and $dv = r^2 dr \sin\theta\, d\theta\, d\phi$, and the fact

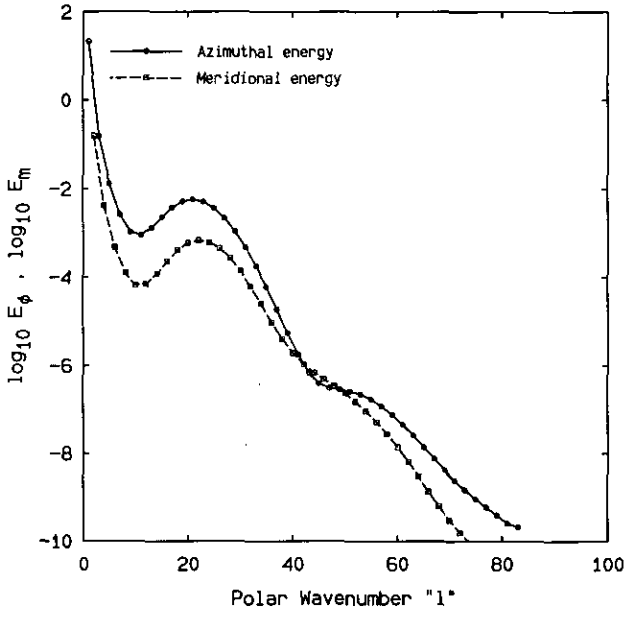

FIG. 4. Azimuthal and meridional energy spectra $E_\phi(l)$ and $E_m(l)$ for the flow field of Fig. 3.

that the velocity expansion (12) reduces for axisymmetric flows to an azimuthal component plus a meridional vector:

$$\begin{aligned} u_\phi(r,\theta)\,\hat{\mathbf{e}}_\phi &= \sum_{l=1}^{L} A_l(r)\,\mathbf{X}_{l,0}(\theta) \\ \mathbf{u}_m(r,\theta) &= \sum_{l=1}^{L} B_l(r)\,\mathbf{V}_{l,0}(\theta) + C_l(r)\,\mathbf{W}_{l,0}(\theta). \end{aligned} \tag{44}$$

It is therefore straightforward to decompose the total kinetic energy of such flows into azimuthal and meridional contributions such that $E = E_\phi + E_m$, and where the *azimuthal spectrum* is given by

$$E_\phi = \sum_{l=1}^{L} E_\phi(l) = \sum_{l=1}^{L} \frac{1}{v}\int_{R_i}^{R_o} \frac{A_l^2}{2} r^2\, dr \tag{45}$$

while the *meridional spectrum* simply reads

$$E_m = \sum_{l=1}^{L} E_m(l) = \sum_{l=1}^{L} \frac{1}{v}\int_{R_i}^{R_o} \left[\frac{B_l^2 + C_l^2}{2}\right] r^2\, dr. \tag{46}$$

For reflection-symmetric flows about the equator, contributions to $E_\phi(l)$ come only from the l = odd modes while those to $E_m(l)$ come solely from the l = even modes as can be seen on the spectra of Fig. 4.

The agreement between our computed solution and Marcus and Tuckerman's is found to be quite good in all respects considered, e.g., qualitative features of the flow field and locations of the critical points undistinguishable (two centers and one saddle per hemisphere), friction torques in agreement better than provided accuracy ($\Upsilon = 2217$), features of the spectra identical including the crossing of E_m over E_ϕ around $l = 45$. Clearly, both numerical simulations have captured all significant motion scales (more than seven decades in the ratio of energy contents between the local maximum and the highest wavenumber) and exhibit exponential decay of the high-wavenumber energy. The local maximum of energy near $l \simeq 23$ corresponds to the polar length-scale of the pinch, i.e., about "0.9d" as seen on Fig. 3 ($l \simeq (\pi R_o)/(0.9d)$). The pinch phenomenon is apparent on both spectra due to the strong correlation observed between the meridional circulation (Ψ) and the azimuthal motion (Ω). The extents and thicknesses of the boundary layers associated with $\mathbf{u}_m$ are clearly shown on the ω_ϕ-contours of Fig. 3, which also provides an alternative means to analyse the important critical points mentioned above [22].

6.2. *Three-Dimensional Flows*

The purpose of our last validation test is to verify the implementation for a three-dimensional computation. The only fully described and quantitatively documented 3D flow

in spherical-gaps is the *narrow-gap spherical Couette flow* after its first transition. Nakabayashi reports in [4] his thorough experimental investigation of that transition, and among other flow regimes, he describes in detail one known as the *spiral Taylor–Görtler vortex flow* (see also [34, 35]).

We select our parameters to match one of Nakabayashi's laboratory cases. The gap-width used is $\delta = 0.06$ ($R_i = 16.667$, $R_o = 17.667$) with the boundary conditions $V_i = 1$ and $V_o = 0$. The critical Reynolds number for that gap, at which Taylor–Görtler vortices first appear, has been determined by flow visualizations as $\mathrm{Re}_c \simeq 166$, in good agreement with infinitely thin-gap theories and cylindrical Couette flow. At $\mathrm{Re} = 195$, i.e., $\mathrm{Re}/\mathrm{Re}_c \simeq 1.17$, the supercritical flow is described by Nakabayashi as a periodic flow exhibiting Taylor vortices whose axes are slightly tilted with respect to the azimuthal direction, hence the appellation "spiral vortices." These vortices can be observed over a $\sim 40°$-region centered at the equator, and are travelling in the azimuthal direction at about 47% of Ω_i (i.e., in that rotating frame, the flow would nearly become steady). Six spiral cells per hemisphere (three of each vorticity sign) have been identified.

We choose for our test simulation the following truncations: $N = 16$, $L = 84$, and $M = 9$ with a physical collocation grid of $33 \times 130 \times 32$ points. The required CPU-time corresponding to this discretization is a quite bearable 12 CPU-s/timestep on a CRAY Y/MP processor. For an actual detailed physical study, an increase of at least 50% in the spherical resolution should be considered based on the fact that a length-scale of order "d" corresponds for this geometry to a polar wavenumber $l_d \sim \pi R_o/d = 55$.

The initial condition used for the simulation was a previously computed subcritical basic solution at $\mathrm{Re} = 160$ to which some very small 3D random noise was added (velocity disturbances less than 10^{-10} in amplitude). Starting with a sudden drop in viscosity leading to $\mathrm{Re} = 195$ at $t = 0^+$, the flow field was marched in time for about six inner-sphere revolutions. At that time, the torque was found to be almost constant ($\Upsilon = 4.81 \times 10^4$ which agrees well with narrow-gaps torque measurements by Wimmer [36]), and the flow had nearly reached a state of steady oscillations.

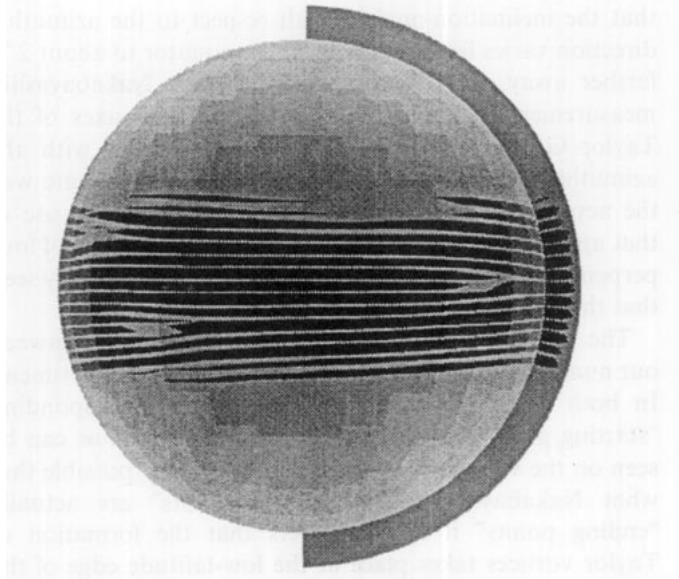

FIG. 5. Visualization of the numerical solution of a spiral Taylor–Görtler vortex flow in a narrow spherical gap $\delta = 0.06$ (enlarged here 3.2 times) with $V_i = 1$, $V_o = 0$, and $\mathrm{Re} = 195$. The radial velocity u_r is shown on a spherical shell at 0.3 gap-width from the inner sphere and on the meridional plane $\phi = 0$. Nonzero velocity appears as dark bands corresponding to radial inflow or outflow regions located in between adjacent Taylor–Görtler vortices. Pale bands, for which $u_r \simeq 0$, correspond to the centers of the vortices.

Qualitatively speaking, our spiral-vortex flow is in very good agreement with the experimental flow of Nakabayashi. Figure 5 shows a numerically produced visualization of the radial sources and sinks associated respectively with the outflow and inflow boundaries between the vortices. The thin pale bands correspond to the axes of the Taylor–Görtler cells. The spiral character of those cells is made clearly visible, and it can be measured

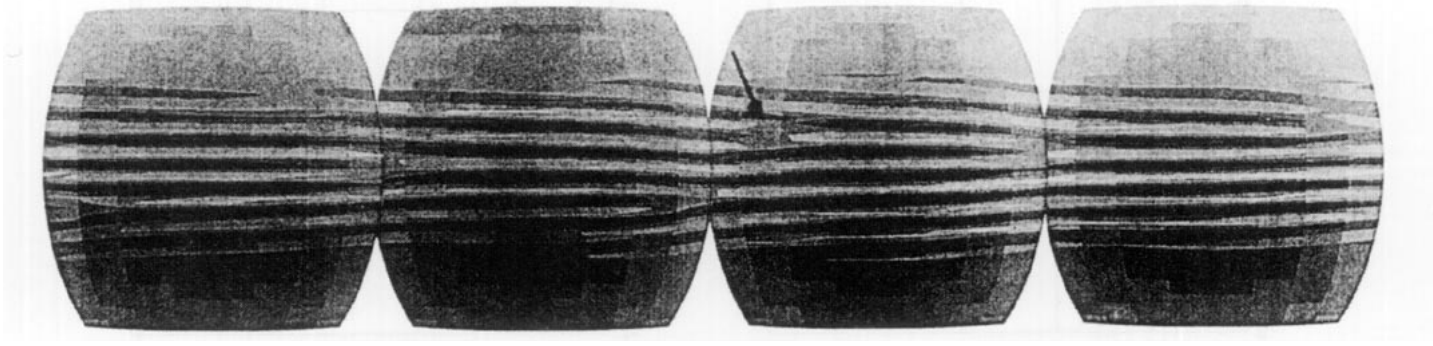

FIG. 6. Visualization of the azimuthal-vorticity field for the spiral-vortex flow of Fig. 5. From left to right, the sequence of colored-surface views corresponds to an observer located at $z = 0$ with respectively $y = -\infty$, $x = \infty$, $y = \infty$, and $x = -\infty$. Dark shade is positive vorticity and pale gray is negative. Note the spiral topology of the vortices as well as the interesting phenomenon of "vortex-branch" (an example of which is indicated by the arrow).

that the inclination-angle α with respect to the azimuthal direction varies from nearly 0° at the equator to about 2.7° farther away. This agrees very well with Nakabayashi's measurements given in Table 3 of [4]. The axes of the Taylor–Görtler vortices being nearly aligned with the azimuthal direction, the ω_ϕ field should approximate well the actual vortex–cell boundaries. Figure 6 makes use of that approximation and shows a revealing montage of four perpendicular views of the equatorial region. It is easily seen that the equator is no longer a symmetry plane.

The number of spiral vortices agrees very well between our numerical computation and Nakabayashi's experiment. In both cases, six spiral cells with three corresponding "starting points" are found in each hemisphere, as can be seen on the visualization. However, it is quite possible that what Nakabayashi calls "starting points" are actually "ending points" if one considers that the formation of Taylor vortices takes place at the low-latitude edge of the basic recirculation cells rather than near the equator [18, 22]. We thus prefer here to call those vortex-splitting regions *vortex-branches*, an example of which is indicated by the arrow on Fig. 6.

Other quantitative comparisons with the experimental flow field have also led to surprisingly good agreements considering the marginal resolution of the present simulation. Among other things, the angular velocity of the spiral vortices, Ω_s, was computed from the Fourier-transformed velocity field at two consecutive times. From the phase shift calculated, we obtain $\Omega_s/\Omega_i = 0.47$. Nakabayashi reports a measured value of 0.466 at our Reynolds number. This implies that the period of the flow is given by $T = 2\pi/\Omega_s = 2.14T_i$ (T_i being the inner-sphere period of revolution) which is consistent with all our computed, point-wise velocity traces.

The energy spectra associated with our 3D spiral Taylor–Görtler vortex flow are provided in Fig. 7. The *Legendre total energy spectrum* is defined as $E(l) \equiv \sum_m E(l, m)$ and the *Fourier total energy spectrum* by $E(m) \equiv \sum_l E(l, m)$, where the VSH discrete energy content $E(l, m)$ is computed in spectral space (from a velocity representation such as Eq. (40)) as

$$E(l, m) = \frac{1}{v} \int_{R_i}^{R_o} \frac{[A_{lm} A_{lm}^* + B_{lm} B_{lm}^* + C_{lm} C_{lm}^*]}{2} r^2 \, dr. \quad (47)$$

The Legendre spectrum $E(l)$ clearly shows a strong local maximum at $l \sim 63$ corresponding to the length-scale $0.88d$ of the spiral vortices present in the flow. This spectrum furthermore indicates that only two decades of decay in energy content is obtained between the local maximum and the tail of spectrum, thus supporting the previous allusion to the marginal level of resolution of the computation. The Fourier spectrum $E(m)$ brings evidence that nine complex modes were indeed sufficient, although marginally, to capture the global features in the azimuthal direction. The weak local maximum at $m = 3$ corresponds to the presence of three pairs of spiral cells per hemisphere.

Figure 8 finally presents a comparison between the meridional streamlines of the axisymmetric part of the actual 3D spiral flow (Fourier mode "$m = 0$") versus the axisymmetrically computed flow (with $M = 0$ and the same discretization in the other two directions) for the same geometry and the same Reynolds number. The latter is found to be a slowly varying periodic flow that exhibits 8 to

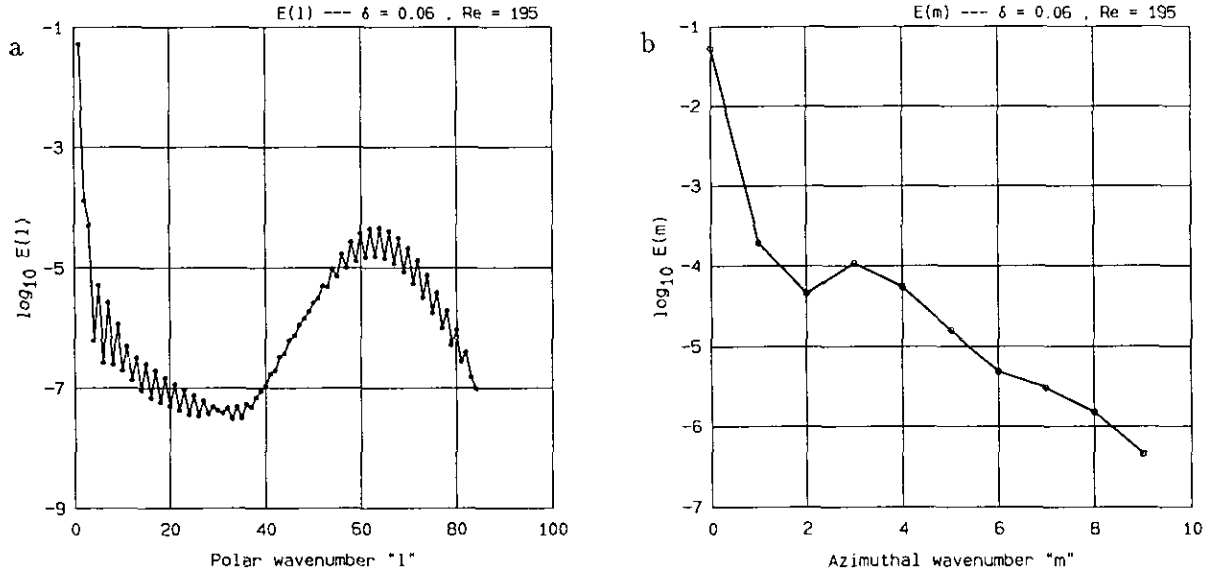

FIG. 7. Energy spectra of the spiral-vortex flow of Figs. 5–6: (a) Legendre-total-energy spectrum $E(l)$; (b) Fourier-total-energy spectrum $E(m)$. The local maximum in $E(l)$ at $l \simeq 63$ corresponds to a length-scale of about "$0.9d$," i.e., the characteristic size of the Taylor–Görtler vortices.

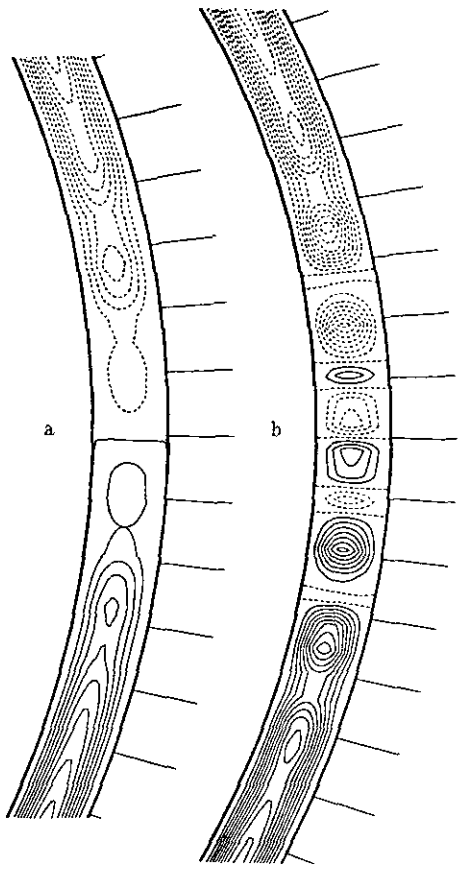

FIG. 8. Meridional streamlines in the equatorial region for (a) the axisymmetric part (Fourier mode "$m=0$") of the 3D vortex-flow solution of Figs. 5–7, and for (b) the axisymmetric, time-periodic flow computed for the same conditions (except with $M=0$) and shown here at $t=1800$. The width of the gap is shown above to scale.

12 Taylor vortices in agreement with the axisymmetric computations of Bartels [37]. It is illustrated here at a time just after the disappearance of the two extreme vortex pairs. One observes from Fig. 8a that no indication of clearly defined axisymmetric vortices is visible in our 3D spiral flow. Thus we see no evidence for the existence of a pair of toroidal vortices at the equator as reported by Nakabayashi. It may be possible that the inclination angle near the equator is too small for reliable experimental determination by the aluminum-flake method of visualization, or that some interference is present due to the fact that the experimental setup has a support post for the inner sphere. A better resolved numerical simulation may help clarify this point.

7. CONCLUSIONS

A spectral method based on divergence-free vector expansions has been presented for the solution of the incompressible Navier–Stokes equations in spherical-gap geometries. No rotational nor equatorial symmetry of the flow field has been implicitly assumed. Chebyshev polynomials are used to construct sets of quasi-orthogonal functions in the radial direction while vector spherical harmonics are chosen for the orthogonal vector functions in the spherical directions. The method is thus characterized by a resolution that is radially concentrated near the solid walls and uniform over spherical shells. It offers the following advantages: (i) spectral convergence; (ii) exact treatment of the continuity equation and boundary conditions; (iii) pressure eliminated as an explicit variable; (iv) only two degrees of freedom per spectral mode; (v) simple and standard time-marching procedure; (vi) implicit treatment of viscous term at no extra cost.

The efficient implementation of the initial-boundary-value code is briefly discussed including the development of a VSH–Chebyshev transform with two fast directions. Fully spectral simulations are warranted by the removal of aliasing errors through the "3/2 rule."

Test cases are presented to validate the method. Several axisymmetric, basic spherical Couette flows are computed and compared with available numerical results. A three-dimensional, spiral Taylor–Görtler vortex flow is also computed and compared with experimental measurements and visualizations. In all cases, the agreement obtained is very good. The method has since been used very successfully in an ongoing study of the transition mechanisms in moderate and in large-gap spherical Couette flows.

APPENDIX A: SPHERICAL HARMONICS

A.1. *Scalar Spherical Harmonics*

$$Y_l^m(\theta,\phi)=\Theta_l^m(\theta)\,e^{im\phi} \tag{A.1}$$

$$\theta_l^m(\theta)=\left(\frac{(2l+1)\,(l-m)!}{4\pi\,(l+m)!}\right)^{1/2}P_l^m(\cos\theta),\qquad |m|\leqslant l \tag{A.2}$$

$$\left.\begin{aligned} P_l^m(\mu)&=(-1)^m\,(1-\mu^2)^{m/2}\frac{d^m}{d\mu^m}P_l(\mu),\\ \mu&\equiv\cos\theta,\quad m\geqslant 0\end{aligned}\right\} \tag{A.3}$$

$$Y_l^{-m}(\theta,\phi)=(-1)^m\,[Y_l^m(\theta,\phi)]^* \tag{A.4}$$

$$\int_0^{2\pi}\int_0^{\pi}Y_l^m(\theta,\phi)\left[Y_{l'}^{m'}(\theta,\phi)\right]^*\sin\theta\,d\theta\,d\phi=\delta_{ll'}\delta_{mm'} \tag{A.5}$$

$$\nabla^2 Y_l^m(\theta,\phi)=-l(l+1)\,Y_l^m(\theta,\phi) \tag{A.6}$$

$$\frac{\partial Y_l^m}{\partial\theta}=\left\{\begin{aligned}&-\frac{1}{2}\left[(l+m)(l-m+1)\right]^{1/2}Y_l^{m-1}\quad e^{i\phi}\\&+\frac{1}{2}\left[(l-m)(l+m+1)\right]^{1/2}Y_l^{m+1}e^{-i\phi}\end{aligned}\right\} \tag{A.7}$$

$$\frac{m}{\sin\theta}\,Y_l^m = \left\{ \begin{array}{l} -\frac{1}{2}\left(\frac{2l+1}{2l+3}\right)^{1/2} \\ \quad \times \left\{ \left[(l+m+2)(l+m+1) \right]^{1/2} \right. \\ \qquad \times Y_{l+1}^{m+1} e^{-i\phi} \\ \quad + \left[(l-m+2)(l-m+1) \right]^{1/2} \\ \qquad \left. \times Y_{l+1}^{m-1} e^{i\phi} \right\} \end{array} \right\}. \quad \text{(A.8)}$$

A.2. *Vector Spherical Harmonics*

Hill's VSH [11]:

$$\begin{aligned} \mathbf{X}_{l,m}(\theta,\phi) &\equiv \frac{-i}{[l(l+1)]^{1/2}} \left[\hat{\mathbf{e}}_r \times (r\,\nabla Y_l^m) \right] \\ \mathbf{V}_{l,m}(\theta,\phi) &\equiv \frac{1}{[(l+1)(2l+1)]^{1/2}} \left[r\,\nabla Y_l^m - (l+1)\,Y_l^m\,\hat{\mathbf{e}}_r \right] \\ \mathbf{W}_{l,m}(\theta,\phi) &\equiv \frac{1}{[l(2l+1)]^{1/2}} \left[r\,\nabla Y_l^m + l\;Y_l^m\,\hat{\mathbf{e}}_r \right] \end{aligned} \quad \text{(A.9)}$$

$$\begin{aligned} \mathbf{X}_{l,-m} &= (-1)^{m+1}\,[\mathbf{X}_{l,m}]^* \\ \mathbf{V}_{l,-m} &= (-1)^m\,[\mathbf{V}_{l,m}]^* \\ \mathbf{W}_{l,-m} &= (-1)^m\,[\mathbf{W}_{l,m}]^* \end{aligned} \quad \text{(A.10)}$$

$$\begin{aligned} r^2\,\nabla^2 \mathbf{X}_{l,m} &= -l(l+1)\,\mathbf{X}_{l,m} \\ r^2\,\nabla^2 \mathbf{V}_{l,m} &= -(l+2)(l+1)\,\mathbf{V}_{l,m} \\ r^2\,\nabla^2 \mathbf{W}_{l,m} &= -l(l-1)\,\mathbf{W}_{l,m} \end{aligned} \quad \text{(A.11)}$$

$$\begin{aligned} \mathbf{X}_{l,m}(\theta,\phi) &= \boldsymbol{X}_{l,m}(\theta)\,e^{im\phi} \\ \mathbf{V}_{l,m}(\theta,\phi) &= \boldsymbol{V}_{l,m}(\theta)\,e^{im\phi} \\ \mathbf{W}_{l,m}(\theta,\phi) &= \boldsymbol{W}_{l,m}(\theta)\,e^{im\phi} \end{aligned} \quad \text{(A.12)}$$

$$\boldsymbol{X}_{l,m}(\theta) = \left\{ \begin{array}{l} [a_l^m \Theta_{l+1}^{m+1} + b_l^m \Theta_{l+1}^{m-1}]\;\hat{\mathbf{e}}_\theta \\ + i[c_l^m \Theta_l^{m-1} + d_l^m \Theta_l^{m+1}]\;\hat{\mathbf{e}}_\phi \end{array} \right\} \quad \text{(A.13)}$$

$$\boldsymbol{V}_{l,m}(\theta) = \left\{ \begin{array}{l} [e_l^m \Theta_l^m]\;\hat{\mathbf{e}}_r \\ + [f_l^m \Theta_l^{m-1} + g_l^m \Theta_l^{m+1}]\;\hat{\mathbf{e}}_\theta \\ + i[h_l^m \Theta_{l+1}^{m+1} + i_l^m \Theta_{l+1}^{m-1}]\;\hat{\mathbf{e}}_\phi \end{array} \right\} \quad \text{(A.14)}$$

$$\boldsymbol{W}_{l,m}(\theta) = \left\{ \begin{array}{l} [j_l^m \Theta_l^m]\;\hat{\mathbf{e}}_r \\ + [k_l^m \Theta_l^{m-1} + p_l^m \Theta_l^{m+1}]\;\hat{\mathbf{e}}_\theta \\ + i[q_l^m \Theta_{l+1}^{m+1} + r_l^m \Theta_{l+1}^{m-1}]\;\hat{\mathbf{e}}_\phi \end{array} \right\}. \quad \text{(A.15)}$$

See Appendix A of Dumas [18] for the explicit definitions of the real indexed coefficients a to r.

Below, $R(r)$ is an arbitrary function of r:

$$\begin{aligned} \nabla\cdot[R(r)\,\mathbf{X}_{l,m}] &= 0 \\ \nabla\cdot[R(r)\,\mathbf{V}_{l,m}] &= -\left(\frac{l+1}{2l+1}\right)^{1/2}\left[\frac{dR}{dr} + \frac{l+2}{r}R\right] Y_l^m \\ \nabla\cdot[R(r)\,\mathbf{W}_{l,m}] &= \left(\frac{l}{2l+1}\right)^{1/2}\left[\frac{dR}{dr} - \frac{l-1}{r}R\right] Y_l^m \end{aligned} \quad \text{(A.16)}$$

$$\nabla\times[R(r)\,\mathbf{X}_{l,m}] = \left\{ \begin{array}{l} i\left(\frac{l}{2l+1}\right)^{1/2}\left[\frac{dR}{dr} - \frac{l}{r}R\right]\mathbf{V}_{l,m} + \\ i\left(\frac{l+1}{2l+1}\right)^{1/2}\left[\frac{dR}{dr} + \frac{l+1}{r}R\right]\mathbf{W}_{l,m} \end{array} \right\} \quad \text{(A.17)}$$

$$\begin{aligned} \nabla\times[R(r)\,\mathbf{V}_{l,m}] &= i\left(\frac{l}{2l+1}\right)^{1/2}\left[\frac{dR}{dr} + \frac{l+2}{r}R\right]\mathbf{X}_{l,m} \\ \nabla\times[R(r)\,\mathbf{W}_{l,m}] &= i\left(\frac{l+1}{2l+1}\right)^{1/2}\left[\frac{dR}{dr} - \frac{l-1}{r}R\right]\mathbf{X}_{l,m} \end{aligned}$$

$$\begin{aligned} \nabla^2[R(r)\,\mathbf{X}_{l,m}] &= \mathscr{L}_l(R)\,\mathbf{X}_{l,m} \\ \nabla^2[R(r)\,\mathbf{V}_{l,m}] &= \mathscr{L}_{l+1}(R)\,\mathbf{V}_{l,m} \\ \nabla^2[R(r)\,\mathbf{W}_{l,m}] &= \mathscr{L}_{l-1}(R)\,\mathbf{W}_{l,m}, \end{aligned} \quad \text{(A.18)}$$

where

$$\mathscr{L}_l \equiv \frac{d^2}{dr^2} + \frac{2}{r}\frac{d}{dr} - \frac{l(l+1)}{r^2}. \quad \text{(A.19)}$$

APPENDIX B: SUMMARY OF SPATIAL DISCRETIZATION

Velocity Expansion (divergence-free)

$$\begin{aligned} &\mathbf{u}(r,\theta,\phi,t) = \\ &\sum_{n=0}^{N}\sum_{l=0}^{L}\sum_{m=-l}^{l}\left\{ \begin{array}{l} a_{nlm}^-(t)\,h_n^-(r)\,\mathbf{X}_{l,m}(\theta,\phi) \\ + a_{nlm}^+(t)\nabla\times[h_n^+(r)\,\mathbf{X}_{l,m}(\theta,\phi)] \end{array} \right\} \\ &\quad + \sum_{m=-1}^{1}\left[\Lambda_m^0(t)\,T_0(\xi) + \Lambda_m^1(t)\,T_1(\xi)\right]\mathbf{X}_{1,m}(\theta,\phi). \end{aligned} \quad \text{(B.1)}$$

Semi-discrete Systems (two systems per couple "l, m")

$$\begin{aligned} &\left[\mathscr{A}_{n'n}^{\pm}\right]_l \left\{\dot{a}_n^{\pm}\right\}_{lm} - \frac{1}{\mathrm{Re}}\left[\mathscr{B}_{n'n}^{\pm}\right]_l \left\{a_n^{\pm}\right\}_{lm} \\ &\quad = \left\{\mathscr{F}_{n'}^{\pm}\right\}_{lm} - \left\{T_{n'}^{bc-}\right\}_m \delta_{l,1} + \frac{1}{\mathrm{Re}}\left\{V_{n'}^{bc-}\right\}_m \delta_{l,1} \end{aligned} \quad \text{(B.2)}$$

$$\mathscr{A}_{n'n}^- = \int_{R_i}^{R_o} h_n^-\,g_{n'}^-\,r^2\,dr$$

$$\mathscr{B}_{n'n}^- = \int_{R_i}^{R_o} \mathscr{L}_l(h_n^-)\,g_{n'}^-\,r^2\,dr$$

$$\mathscr{A}^{+}_{n'n} = \int_{R_i}^{R_o} [h^{+V}_{nl} g^{+V}_{n'l} + h^{+W}_{nl} g^{+W}_{n'l}] \, r^2 \, dr$$

$$\mathscr{B}^{+}_{n'n} = \int_{R_i}^{R_o} [\mathscr{L}_{l+1}(h^{+V}_{nl}) \, g^{+V}_{n'l} + \mathscr{L}_{l-1}(h^{+W}_{nl}) \, g^{+W}_{n'l}] \, r^2 \, dr$$

$$\mathscr{F}^{-}_{n'} = \int_{R_i}^{R_o} f^{X}(r) \, g^{-}_{n'} \, r^2 \, dr$$

$$\mathscr{F}^{+}_{n'} = \int_{R_i}^{R_o} [f^{V}(r) \, g^{+V}_{n'l} + f^{W}(r) \, g^{+W}_{n'l}] \, r^2 \, dr$$

$T^{bc-}_{n'}$, $V^{bc-}_{n'}$: Eq. (36); $A^{0,\pm 1}_{m}(t)$: Eq. (35)

$$\mathscr{L}_l \equiv \frac{d^2}{dr^2} + \frac{2}{r}\frac{d}{dr} - \frac{l(l+1)}{r^2}.$$

$$h^{+V}_{nl}(r) = i\left(\frac{l}{2l+1}\right)^{1/2}\left[\frac{dh^{+}_{n}}{dr} - \frac{l}{r} h^{+}_{n}\right];$$

$$h^{+W}_{nl}(r) = i\left(\frac{l+1}{2l+1}\right)^{1/2}\left[\frac{dh^{+}_{n}}{dr} + \frac{l+1}{r} h^{+}_{n}\right];$$

$$g^{+V}_{n'l}(r) = -i\left(\frac{l}{2l+1}\right)^{1/2}\left[\frac{dg^{+}_{n'}}{dr} - \frac{l}{r} g^{+}_{n'}\right];$$

$$g^{+W}_{n'l}(r) = -i\left(\frac{l+1}{2l+1}\right)^{1/2}\left[\frac{dg^{+}_{n'}}{dr} + \frac{l+1}{r} g^{+}_{n'}\right];$$

$$h^{-}_{n}(r(\xi)) = (1-\xi^2) \, T_n(\xi);$$

$$h^{+}_{n}(r(\xi)) = (1-\xi^2)^2 \, r \; T_n(\xi);$$

$$g^{-}_{n'}(r(\xi)) = \frac{1}{(1-\xi^2)^{1/2}} (1-\xi^2) \, T_{n'}(\xi);$$

$$g^{+}_{n'}(r(\xi)) = \frac{1}{(1-\xi^2)^{1/2}} (1-\xi^2)^2 \, r \; T_{n'}(\xi);$$

$$\xi = 2r - K \;\leftrightarrow\; r = \frac{1}{2}(\xi + K);$$

$T_n(\xi)$: nth degree Chebyshev polynomial;

$\mathbf{X}_{l,m}$, $\mathbf{V}_{l,m}$, $\mathbf{W}_{l,m}$: VSHs of degree l, order m.

ACKNOWLEDGMENTS

This work was partially supported by the Office of Naval Research. One of us [G.D.] would like to thank the NSERC of Canada and the FCAR of Québec for their financial support. The San Diego Supercomputer Center, CA, is gratefully acknowledged for providing the computing ressources necessary for this work.

REFERENCES

1. A. Leonard and A. Wray, in *8th Int. Conf. on Numer. Methods in Fluid Dyn., Aachen, W. Germany, June 1982.*
2. G. A. Glatzmaier, *J. Comput. Phys.* **55**, 461 (1984).
3. M. Wimmer, *Prog. Aerosp. Sci.* **25**, 43 (1988).
4. K. Nakabayashi, *J. Fluid Mech.* **132**, 209 (1983).
5. I. M. Yavorskaya, Y. N. Belyaev, A. A. Monakhov, N. M. Astaf'eva, S. A. Scherbakov, and N. D. Vvedenskaya, "Stability, Non-uniqueness and Transition to Turbulence in the Flow between Two Rotating Spheres," in *Proceedings, XVth Int. Cong. of Theor. and Appl. Mech., IUTAM, Toronto, Canada, 1980*, p. 431.
6. P. S. Marcus and L. S. Tuckerman, *J. Fluid Mech.* **185**, 1 (1987).
7. K. Bühler, *Acta Mech.* **81**, 3 (1990).
8. R. D. Moser and P. Moin, Report No. TF-20, Thermosciences Div., Stanford University, July 1984 (unpublished).
9. P. R. Spalart, NASA TM-88222. Feb. 1986 (unpublished).
10. S. K. Stanaway, B. J. Cantwell, and P. R. Spalart, "Navier–Stokes Simulations of Axisymmetric Vortex Rings," in *AIAA-88-0318, 26th Aerospace Sciences Meeting, Reno, Nevada, January 1988.*
11. E. L. Hill, *Am. J. Physics* **22**, 211 (1953).
12. C. Canuto, M. Y. Hussaini, A. Quarteroni, T. A. Zang, *Spectral Methods in Fluid Dynamics*, (Springer-Verlag, Berlin, 1987).
13. S. K. Stanaway, B. J. Cantwell, and P. R. Spalart, "A Full Simulation of a Vortex Ring," in *Ninth Australasian Fluid Mechanics Conference. Auckland, New Zealand, December 1986.*
14. S. A. Orszag, *Mon. Weather Rev.* **102**, 56 (1974).
15. L. Fox and I. B. Parker, *Chebyshev Polynomials in Numerical Analysis*, Oxford Math. Handbooks (Oxford Univ. Press, London, 1968).
16. F. Pasquarelli, A. Quarteroni, and G. Sacchi-Landriani, *J. Sci. Comput.* **2** (3), 195 (1987).
17. R. D. Moser, P. Moin, and A. Leonard, *J. Comput. Phys.* **52**, 524 (1983).
18. G. Dumas, Ph.D. dissertation, GALCIT Laboratory, California Institute of Technology, 1991.
19. D. Gottlieb and S. A. Orszag, *Numerical Analysis of Spectral Methods*, NSF-CMBS Monograph 26 (SIAM, Philadelphia, 1977).
20. S. A. Orszag, *J. Comput. Phys.* **37**, 70 (1980).
21. W. H. Press, B. P. Flannery, S. A. Teukolsky, and W. T. Vetterling, *Numerical Recipes* (Cambridge Univ. Press, Cambridge, 1986).
22. G. Dumas, and A. Leonard, in preparation.
23. C. E. Pearson, *J. Fluid Mech.* **28**, 323 (1967).
24. B. R. Munson and D. D. Joseph, *J. Fluid Mech.* **49**, 289 (1971).
25. D. Greenspan, *Comput. Fluids* **3**, 69 (1975).
26. D. Schultz and D. Greenspan, *Comput. Fluids* **7**, 157 (1979).
27. S. C. R. Dennis and L. Quartapelle, *Comput. Fluids* **12**, 77 (1984).
28. J.-K. Yang, Ph.D. dissertation, Marquette University, 1987.
29. S. Schwengels, D. Schult, and W. Shay, *Int. J. Numer. Methods Fluids* **9**, 1099 (1989).
30. J. C. Gagliardi, N. J. Nigro, A. F. Elkouch, J. K. Yang, and L. Rodriguez, *J. Eng. Math.* **24**, 1 (1990).
31. S. C. R. Dennis and S. N. Singh, *J. Comput. Phys.* **28**, 297 (1978).
32. L. S. Tuckerman, Ph.D. dissertation, Massachusetts Institute of Technology, Nov. 1983.
33. G. Schrauf, *J. Fluid Mech.* **166**, 287 (1986).
34. K. Nakabayashi, *Trans. ASME, J. Fluids Eng.* **100**, 97 (1978).
35. J. Zierep and O. Sawatzki, (1970): "Three-Dimensional Instabilities and Vortices between Two Rotating Spheres," in *Eight Symp. Naval Hydrodynamics, Pasadena, CA, August 1970*, p. 275.
36. M. Wimmer, *J. Fluid Mech.* **78**, 317 (1976).
37. F. Bartels, *J. Fluid Mech.* **119**, 1 (1982).
38. P. R. Spalart, R. D. Moser, and M. M. Rogers, *J. Comput. Phys.* **96**, 297 (1991).
39. S. C. R. Dennis and L. Quartapelle, *J. Comput. Phys.* **61**, 218 (1985).